Journal of the Serbian Society for Computational Mechanics / Vol. 16 / No. 1, 2022 / pp 1-15
(10.24874/jsscm.2022.16.01.01)

EXPERIMENTAL AND NUMERICAL INVESTIGATIONS OF A TURBULENT BOUNDARY LAYER UNDER VARIABLE TEMPERATURE GRADIENTS

Amar Berkache[1], Salah Amroune[1,2,*], Ali Golbaf[3], Barhm Mohamad[4]

[1] Faculty of Technology, Mohamed Boudiaf University M'sila Algeria, 28000
e-mail: amar.berkache@univ-msila.dz**,** salah.amroune@univ-msila.dz
[2] Laboratoire de Matériaux et Mécanique des Structures (LMMS), Université de M'sila, Algérie
[3] Faculty of Mechanical Engineering, University of Guilan, Rasht, Iran
e-mail: ali.golbaf71@gmail.com
[4] Department of Petroleum Technology, Koya Technical Institute, Erbil Polytechnic University, 44001 Erbil, Iraq
e-mail: pywand@gmail.com
**corresponding author*

Abstract

In this article we present an experimental and numerical study of the behavior of the boundary layer type viscous flow in the presence of the thermal effect. The flow was held in a three-dimensional field with a uniform infinite velocity in the case of an adiabatic wall with heat input. The presented experimental work was performed in the Thermal Laboratory (LET) of the Prime Institute of Poitiers (France). It describes the analysis of a turbulent boundary layer created in a wind tunnel on the surface of a flat plate covered with epoxy resin. An HP 6012A power supply system was used to provide circulating heat flux to heat the flat plate to 80°C by the Joule effect. The numerical result shows a clear difference in the evolution of the thermal boundary layer between the three temperatures of the wall.

Keywords: Infinite velocity, turbulent boundary layer, temperature gradient, heat flux, fluent.

1. Introduction

The analysis of wall turbulence presents significant challenges both experimentally and numerically. Recently, a novel experimental approach employing hot wire anemometry and particle image velocimetry has been introduced to investigate the turbulent boundary layer of flat plates at high Reynolds numbers. These approaches not only have allowed access to classical results and validation of the device but also have provided the first contribution to the understanding of the organization of the parietal production zone (Brooks et al., 2018). Although, the hot wire anemometer has been firstly used to characterize the Reynolds tensor and to present energy spectra in the turbulent boundary layer, the determination of the average properties by statistical methods provides little information on the structures participating in the organization of turbulence. These structures have been discovered mainly by flow visualization methods (Klebanoff 1955). Theodorsen Theodore (Theodorsen 1959) is the first who proposed the

existence of hairpin vortices. It has been proven that the formation of streaks near the wall and the bursting phenomenon are the main reasons for the production of turbulence (Kline et al., 1967).

Falco R. (Falco 1983) observed the presence of vortices bearing his name on the interface of the turbulent boundary layer. All proposed processes of self-generation of turbulence. In particular, Falco R. (Falco 1983) considered the interaction of the vortices of (Falco 1983) and the wall, and (Head et al., 1981) with a distribution of hairpin vortices. (Blackwelder et al., 1976) and (Wallace et al., 1972) tried using detection methods such as VITA or the Quadrants method to identify and quantify these coherent structures without really succeeding.

In recent years, the appearance of new techniques has provided the scientific community with access to new information about turbulence. Firstly, Direct Numerical Simulation (DNS) which, for low Reynolds numbers, allows a three-dimensional resolution of the flow. Robinson (Robinson 1991) was thus able, due to the data of Spalart 12, to find the hairpin vortices by visualizing the isobars. These results can now be compared to those obtained by Particle Image Velocimetry (PIV). Using this method, Kähler's team (Kähler et al., 1998) observed a cross-section of these vortices.

The main objectives of the experiment were to calculate the turbulence via the RMS velocity, the evolution of the aerodynamic and thermal boundary layer and the effect of the temperature gradient on the thermal boundary layer. Measurements were made along the plate following the X axis in the downstream direction of the flow. Six measurement stations were chosen, ranging from X = 0 to X = 180 mm. At inlet conditions (X = 0), the free flow velocity Ue = 2.3m / s, Re = 33600 and Te = 40 ° C.

2. Dynamic and thermal boundary layer

2.1 Concept of boundary layer

The unsteady full-potential equation written in a body-fitted coordinate system is given to consider the flow of a fluid with a speed U_∞ at velocity at the infinite, and a temperature T_∞ on a flat plate at a temperature Tp. In the vicinity of the wall, the values of the velocity and the temperature are different from those of the potential flow and vary according to the distance to the wall y. This zone of speed and temperature gradients is called the boundary layer (Barhm et al, 2020, Barhm et al, 2019). It results from an exchange of momentum and heat between the fluid and the wall. Its thickness is generally small compared to the entire flow. There are two types of boundary layer: the dynamic boundary layers and the thermal boundary layer.

2.2 Dynamic boundary layer

One of the main characteristics of a fluid is viscosity. It varies with temperature and never vanishes. At the wall, the velocity of the fluid is zero, and friction forces are observed. As it is depicted in Figure 1, these forces slow the flow in the vicinity of the wall.

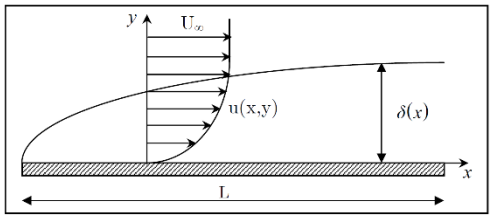

Fig. 1. Variation of the thickness and velocity of the dynamic boundary layer on a flat plane.

2.3 Thermal boundary layer

When a fluid, at temperature T∞, flows over a wall at temperature Tp, heat exchange is established. Fluid particles heat up or cool down in contact with the wall. These particles exchange heat gradually with their neighbors and as it is shown in Figure 2, a temperature gradient is formed.

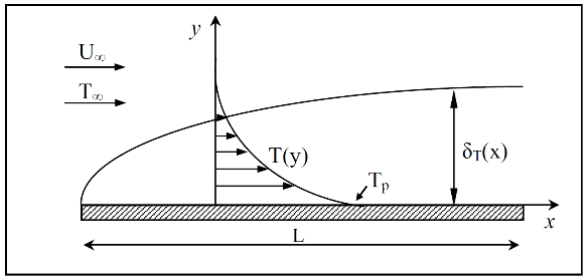

Fig. 2. Thermal boundary layer on a flat plate.

2.4 Characteristic parameters of boundary layer

2.4.1 Dynamic boundary layer thickness

U and $U_e(x)$ are the velocities obtained for a perfect fluid on the flat plate. The conventional boundary layer thickness is equal to the transverse distance where the longitudinal component of the velocity reaches 99% of Ue (x). This scale usually varies with the abscissa along the plate. By denoting it by δ(x), we have (Saeed et al., 2020):

$$U\left[x,\delta\left(x\right)\right]=0.99U_e\left(x\right) \tag{1}$$

2.4.2 Thermal boundary layer thickness

Similarly to the dynamic boundary layer thickness, the thickness of the thermal boundary layer δT is defined. Let the dimensionless report be

$$\frac{T\left(x,y\right)-T_p\left(x\right)}{T_\infty-T_p\left(x\right)} \tag{2}$$

Where T (x,y) is the temperature at the current point of the boundary layer, Tp (x) is that of the wall and T∞ that of fluid away from the wall.
The thermal boundary layer thickness is the transverse distance at the end of which the temperature gap reaches 99% of the difference (T_∞-Tp). So, we have (Saeed et al., 2020)

$$\frac{T\left(x,\delta_T\right)-T_p\left(x\right)}{T_\infty-T_p\left(x\right)}=0.99 \tag{3}$$

2.4.3 Thickness of displacement

Due to the slowing down of the fluid at the wall, the flow of fluid through the boundary layer thickness is less than it would be, at equal distances, in perfect fluid, as shown in Fig. 3. By neglecting the variation of the perfect fluid quantities over a transversal distance of the order of the boundary layer thickness, this deficit can be approximately evaluated by Saeed et al., 2020.

$$q_p-q_v=\int_0^{\delta}\left(\rho_E U_E-\rho U\right)dy \tag{4}$$

By convention, it is expressed from a thickness δ_1 such that:

$$q_p-q_v=\rho_E U_E\delta_1 \tag{5}$$

$$\delta_1\left(x\right)=\int_0^{\infty}\left(1-\frac{\rho U}{\rho_E U_E}\right)dy \tag{6}$$

The thickness δ_1 is called displacement thickness. As illustrated in the figure below, this qualifier refers to the physical interpretation of this quantity, which corresponds to the distance from which the wall should be moved to preserve, in perfect fluid on the thickness (δ - δ1), the same flow rate as viscous fluid over the entire boundary layer section.

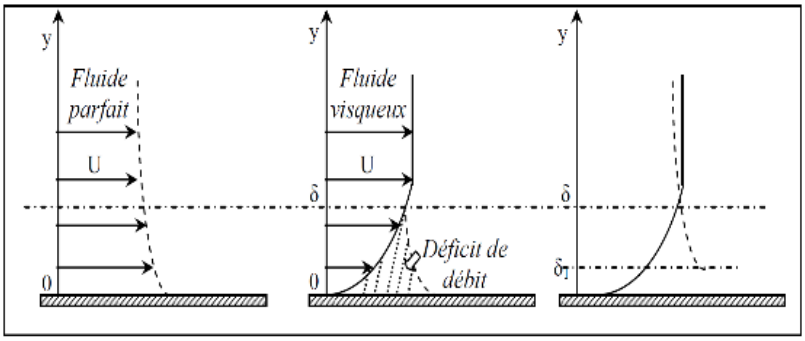

Fig. 3. Flow rate deficit and displacement thickness.

2.4.5 Momentum thickness

The slowing down of the fluid at the wall also results in a lack of momentum. To account for this and in a similar way to the displacement thickness, a second scale called the momentum thickness δ2 is introduced, such as

$$\theta\left(x\right)=\int_0^{\infty}\frac{\rho U}{\rho_E U_E}\left(1-\frac{U}{U_E}\right)dy \tag{7}$$

As for δ_1, this new thickness permits to express the difference in momentum of flow between perfect fluid and viscous fluid with the same mass flow ρU in the form:

$$J_p - J_v \cong \int_0^{\delta} \rho U U_E dy - \int_0^{\infty} \rho U^2 dy \equiv \rho_E U_E^2 \delta_2 \tag{8}$$

3. Problem description

3.1 Experimental study

3.1.1 Experimental facility

Our experimental work focuses on the study of an aerodynamic and thermal boundary layer carried out on a test bench. The temperature of the main flow of air flowing over the flat plate where the boundary layer is formed is equal to 40 °. To vary the temperature of the plate, three heat flow densities corresponding respectively to wall temperatures Tp1=35°C, Tp2=45°C and Tp3=55°C were necessary. These three fluxes were created by an electrical circuit etched on the flat plate covered with a thin layer of epoxy (Fig. 4). An infrared camera was used to measure the temperature field of the injection wall, and the plate was painted black to increase its emissivity ε_p whose value was measured experimentally, and which is equal to 0.95 ± 0.02.

Fig. 4. Experimental facility for measuring the flat plate temperatures.

3.1.2 Study field

The field of study is a rectangular section pipe consisting of four plates: two back and front plates and two lower and upper plates. The back plate that represents the subject injection wall of our study contains perforations. The front wall is a transparent wall to allow measurements. This transparent wall also called the "sounding wall" was pierced and equipped with a porthole to allow the introduction of probes or adjustment measures. The two lower and upper plates connect the other two plates to create the pipe. (Fig. 5).

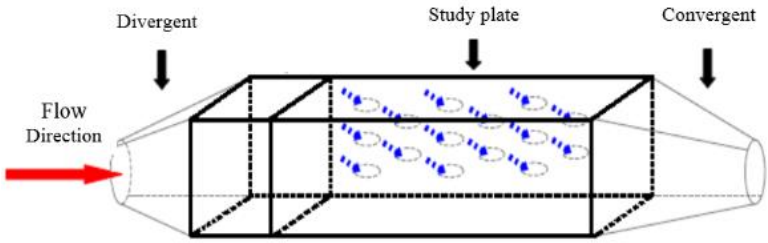

Fig. 5. Schematic representation of the test vein.

The study wall is a plate with dimensions 880x185 mm2 and 1.6 mm thick epoxy resin. (Fig. 6)

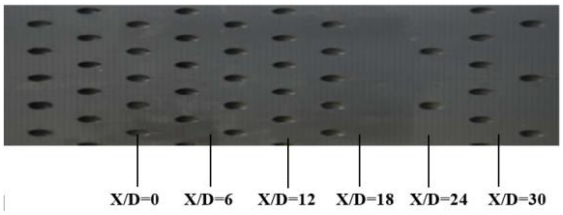

Fig. 6. Photograph of the perforated plate (partial view).

3.1.3 Temperature measurements of the flat plate

To achieve this experimental measurement on the flat plate (not perforated plate), the perforations (81 holes of diameter D) were sealed to prevent the injection flow through the perforations.

The surface temperature measurements of our wall are made by infrared thermography. The infrared camera used is a CEDIP Itanium dot matrix camera. The wall temperatures are computed by a matrix of 320x256 detectors giving us matrices of 256 lines and 320 columns. The position of the infrared camera in our tests is about 0.5 m from the test plate giving a resolution of about 0.25x0.25 mm2 per pixel (Fig. 7)

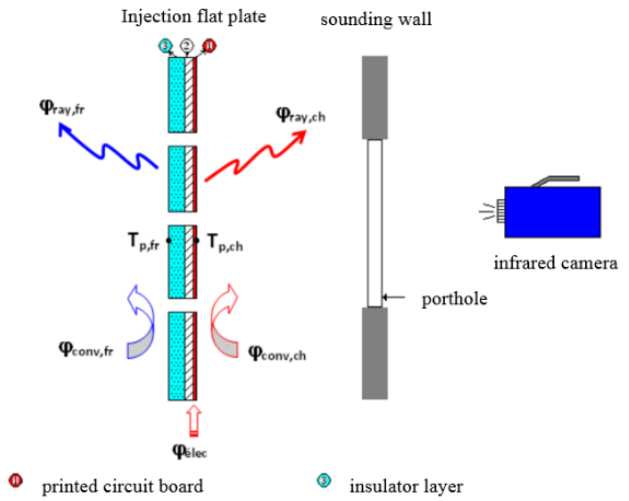

Fig. 7. Camera arrangement for measuring temperatures of the flat plate.

4. Numerical study

A numerical study associated with the experimental study was carried out in order to have more results that could not be realized experimentally, and to be able to compare the numerical results with the experimental results.

4.1 Basic Equations

Two evolution equations are used to describe the flow of an incompressible fluid in its motion. One reflects the mass conservation, the other is the conservation of momentum. The third equation concerns the heat transfer: the energy equation.

4.1.1 Conservation of mass

$$\frac{\partial u_i}{\partial x_i} = O \tag{9}$$

4.1.2 Navier-Stokes incompressible

$$\frac{\partial u_i}{\partial t} + \frac{\partial}{\partial x_j}\left(u_i u_j\right) = -\frac{1}{\rho}\frac{\partial \rho}{\partial x_i} + \frac{\partial}{\partial x_j}(2\nu S_{ij}) + \frac{f_i}{\rho} \tag{10}$$

4.1.3 Heat equation

$$\frac{\partial \mathrm{T}}{\partial \mathrm{t}} + \frac{\partial}{\partial \mathrm{x_j}}\left(\mathrm{u_j T}\right) = \frac{\partial}{\partial \mathrm{x_j}}\left(\alpha_\mathrm{f}\frac{\partial \mathrm{T}}{\partial \mathrm{x_j}}\right) + \mathrm{Q_f} \tag{11}$$

The software utilized is fluent software. FLUENT is a Computational Fluid Dynamics (CFD) code for modelling fluid flow, heat transfer, mass transfer and chemical reactions.

4.2 Model of turbulence

The turbulence model used in our study is the Reynolds Stress Model (RSM), also known as the Reynolds Stress Transport Model, which is a high-level turbulence closure model and represents the classical turbulence model, the most completed one. The closure method employed is usually called a second-order closure. In Reynolds stress models, the turbulent viscosity approach is avoided and the individual components of the Reynolds stress tensor are directly calculated. These models are based on the exact Reynolds constraint transport equation. They can take into account complex interactions in turbulent flow fields, such as the directional effects of Reynolds constraints.

The exact transport equations for the transport of the Reynolds stresses, $\rho\overline{u_i' u_j'}$ may be written as follows:

$$\begin{aligned}
&\frac{\partial}{\partial_t}(\rho\overline{\mathrm{u'_i u'_j}}) + \frac{\partial}{\partial x_k}(\rho\overline{\mathrm{u'_k u'_i u'_j}}) = -\frac{\partial}{\partial x_k}[\rho\overline{\mathrm{u'_i u'_j u'_k}}) + \mathrm{p}(\delta_{\mathrm{kj}}\,\mathrm{u'_i} + \delta_{\mathrm{kj}}\,\mathrm{u'_j})] + \frac{\partial}{\partial x_k}[\mu\frac{\partial}{\partial x_k}(\overline{u'_i\,u'_j})] \\
&-\rho(\overline{u'_i\,u'_k}\frac{\partial u_j}{\partial x_k} + \overline{u'_k\,u'_k}\frac{\partial u_j}{\partial x_k}) - \rho\beta(\mathrm{g_i}\,\overline{\mathrm{u'_j}\,\theta} + \mathrm{g_j}\,\overline{\mathrm{u'_i}\,\theta}) + \overline{\mathrm{p}(\frac{\partial u_i}{\partial x_j} + \frac{\partial u_j}{\partial x_i} - 2\mu\frac{\partial u_i}{\partial x_j}\frac{\partial u_j}{\partial x_i}} \\
&-2\rho\Omega_k(\overline{u'_j\,u'_m}\varepsilon_{ikm} + \overline{u'_i\,u'_m}\varepsilon_{jkm}) + S_{user}
\end{aligned} \tag{12}$$

Where:

$\frac{\partial}{\partial_t}(\rho\overline{u'_i u'_j})$	Local Time Derivative
$\frac{\partial}{\partial x_k}(\rho\overline{u'_k u'_i u'_j})$	$C_{ij} \equiv$ Convection
$\frac{\partial}{\partial x_k}[\rho\overline{u'_i u'_j u'_k}) + p(\delta_{kj} u'_i + \delta_{kj} u'_j)]$	$DT_{ij} \equiv$ Turbulent Diffusion
$\frac{\partial}{\partial x_k}[\mu\frac{\partial}{\partial x_k}(\overline{u'_i u'_j})]$	$DL_{ij} \equiv$ Molecular Diffusion
$\rho(\overline{u'_i u'_k}\frac{\partial u_j}{\partial x_k} + \overline{u'_k u'_k}\frac{\partial u_j}{\partial x_k})$	$P_{ij} \equiv$ Molecular Diffusion
$\rho\beta(g_i \overline{u'_j \theta} + g_j \overline{u'_i \theta})$	$G_{ij} \equiv$ Buoyancy Production
$\overline{p(\frac{\partial u_i}{\partial x_j} + \frac{\partial u_j}{\partial x_i} - 2\mu\frac{\partial u_i}{\partial x_j}\frac{\partial u_j}{\partial x_i}}\ p(\frac{\partial u_i}{\partial x_j} + \frac{\partial u_j}{\partial x_i})$	$\emptyset_{ij} \equiv$ Pressure Strain and $\epsilon_{ij} \equiv$ Dissipation
$-2\rho\Omega_k(\overline{u'_j u'_m}\varepsilon_{ikm} + \overline{u'_i u'_m}\varepsilon_{jkm})$	$F_{ij} \equiv$ Production by System Rotation
S_{user}	$F_{ij} \equiv$ User-Definec Term

The various terms in these exact equations, C_{ij}, D_{Lij} do not require any modeling. However, $G_{ij}, \emptyset_{ij}$ and ϵ_{ij} need to be modeled to close the equations.

4.3 Calculation domain and boundary conditions

The computational domain and the adopted boundary conditions are shown in Fig. 8.

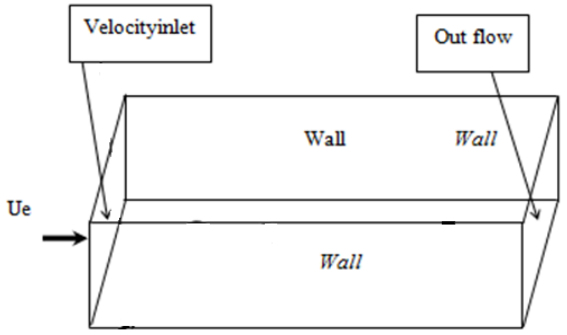

Fig. 8. Computational domain and boundary conditions.

- Speed Ue = 2.3 m / s
- Temperature Te = 40 ° C
- Flow output: Outflow

- Flat plate: Wall with 3 temperatures: Tp = 35 ° C; Tp = 45 ° C and Tp = 55 ° C
- The other faces of the test vein: Wall with a temperature Tw = 22 ° C

4.4Mesh and choice of Y +

The mesh adopted is a tight tetrahedral mesh at the wall and coarse in the far-off environment. Our close wall mesh is correctly chosen to ensure accurate simulation of the flow field. As a result, the height of the first mesh above the necessary plate is calculated to obtain a suitable Y+ using the theory of the boundary layer of the flat plate. The calculations adopted are based on Frank M. White Fluid Mechanics' flat plate boundary layer theory (Frank 2011).

$$Re_x = \frac{\rho U_e . L}{\mu} \tag{13}$$

$$C_f = \frac{0.026}{Re_x^{1/7}} \tag{14}$$

$$T_{wall} = \frac{C_f \rho U_e^2}{2} \tag{15}$$

$$U_{fric} = \sqrt{\frac{T_{wall} y^+ \mu}{\rho}} \tag{16}$$

$$\Delta_s = \frac{C\mu}{U_{fric}\rho} \tag{17}$$

For y+ = 30 and:

- Main flow velocity Ue=2.3 m/s
- Density ρ = 1.225 kg/m3
- Dynamic viscosity μ = 0.000018375 kg/(m•s)
- Reference length L = 0.2 m

We will have

- Height of the first stitch Δs = 0.003 m
- Number of Reynold Rex = 30667

5. Presentation of experimental and numerical results

5.1 Exploitation of experimental results.

5.1.1 Boundary layer thickness δ and momentum thickness θ

Figure 9 illustrates the evolution of the geometric thickness δ of the boundary layer and the thickness θ of the momentum along the X axis. The thickness δ of the boundary layer tends to remain constant at the beginning of the flat plate up to X/D = 6, then it begins to increase in a fast manner with the direction of flow from X/D = 6 to X/D = 10. From this position, the increase of δ is smaller to nevertheless reach a value of 5 mm at X/D = 30. Concerning the thickness of the

momentum, it tends to have the same behavior as the boundary layer thickness because it is proportional to it with some small differences at the beginning of the increase. In the case of the quantity of movement, it begins its increase to X/D = 6 up to X/D = 10 where it changes its rate of increase. From X/D = 10 the evolution of θ loses its rhythm of the increase until reaching a value of 5 kg/s in X/D = 30.

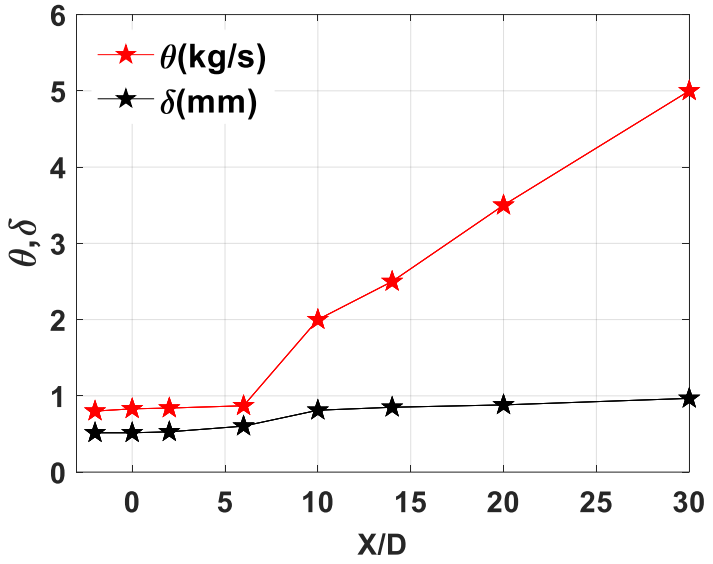

Fig. 9. Evolution of the boundary layer thickness δ and the momentum thickness θ along the X axis.

5.1.2 Intensity of turbulence

Turbulence intensity statistics are presented in terms of rms. The turbulence intensity is represented by the availability of the standard deviations according to X (left column) and Y (right column) in the experiments that were reconstructed by measuring the two components of the fluctuating velocity. The values at the central plane obtained by the experiment are shown in Fig. 10. The maximum value entered for the reduced standard deviation σx/Ue is X/D = 6 where its value reaches 0.23 and σy/Ue = 0.12. From X/D = 18, we notice slight stability of the standard deviations σx and σy.

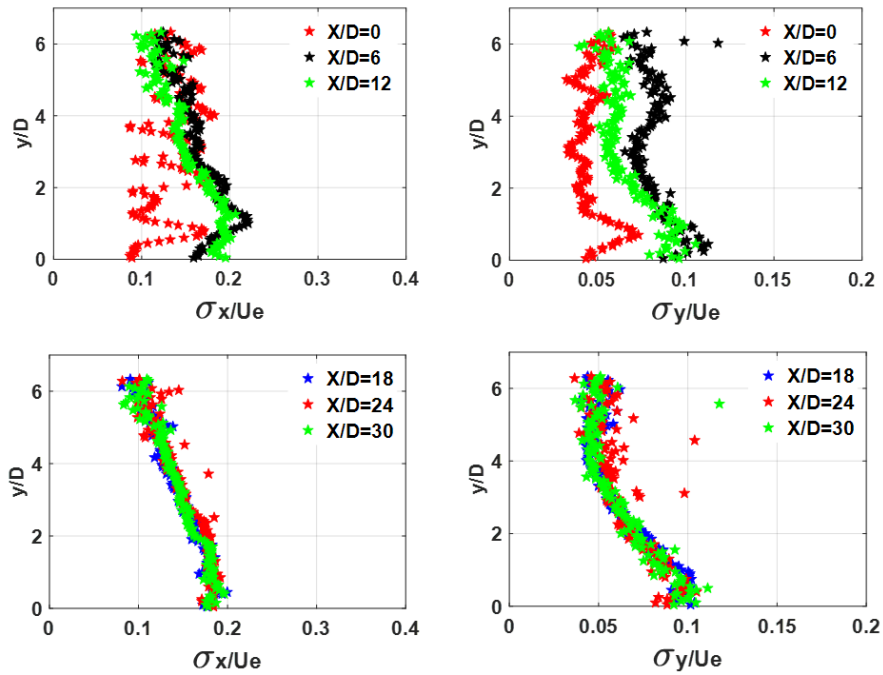

Fig. 10. Profiles of standard deviations in longitudinal and vertical directions depending on the position of X/D = 0 to X/D = 30.

Figure 11 shows the contours of the standard deviations in the longitudinal (a) and vertical (b) directions as a function of the position of X/D=0 to X/D=30. Two main areas of turbulence generation are identified in this figure. The first zone is just above the wall, with turbulence levels from about 40% at about Y/D = 2 of X/D = 5 at X/D = 30 for σx and X/D = 0 to X/D = 30 for σy.

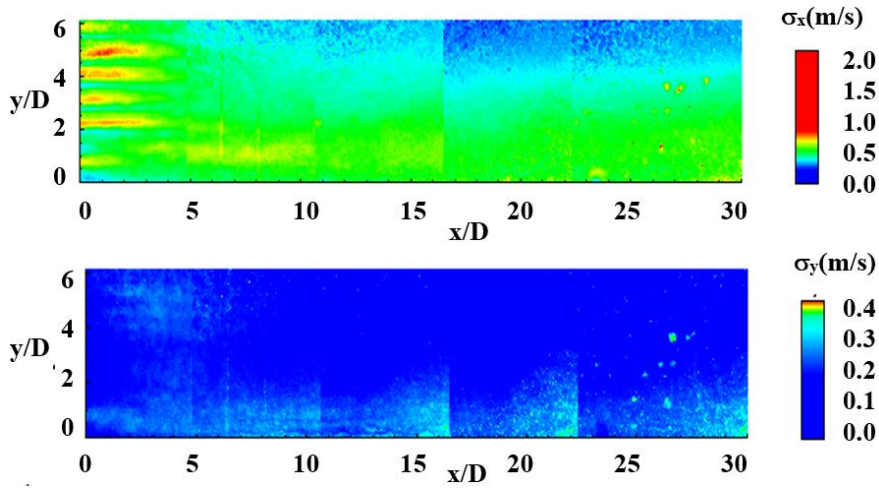

Fig. 11. Contours of standard deviations in two directions: longitudinal (a)and vertical (b) as a function of the position of X/D = 0 to X/D = 30.

5.2 Exploitation of numerical results.

5.2.1 Sensitivity to mesh: Profiles of average speeds U. Comparison with experience

Figure 12 shows the results of the longitudinal velocity profiles obtained by three distinct meshes: Large mesh (251656 meshes), Medium Mesh (703333 meshes) and fine Mesh (1696077 meshes) in different longitudinal stations (X/D=0 mm, X/D=6, X/D=12, X/D=18, X/D=24, X/D=30) along the X axis in the central longitudinal plane. The mesh is tight at the wall and the injection ports. Note that the coarse mesh gives poor results far from the experimental results, while the mean mesh and the fine mesh give almost the same result closer to those obtained by the experiment in all computation stations, especially in the near-wall. For this reason, we used the average mesh for the following calculations in order to save computing time.

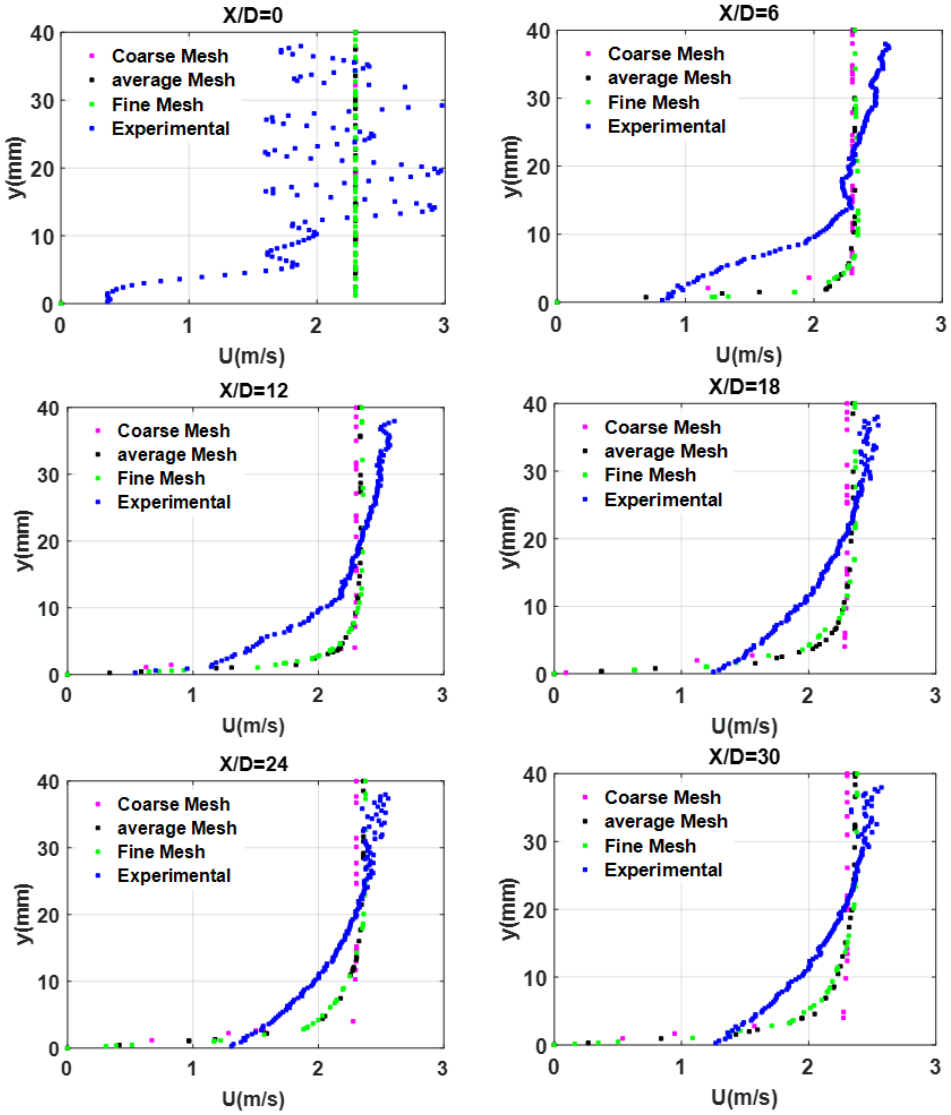

Fig. 12. Longitudinal velocity profiles obtained by three distinct meshes.

5.2.2 Static temperature profiles for three different flat plate temperatures

Figure 13 shows the variation of the thermal boundary layer in terms of the variation of the reduced static temperature T(δT)/Te for three different values of the temperature of the flat plate, subject of our study; Tp=35°C (308K), Tp=45°C (318K) and Tp=55°C (328K) depending on the reduced height of our test vein Y Where H=0.2m represents the total height of the vein. The temperature Te of the main flow or temperature at infinity T∞ has been set at 40°C (313K). A gradual increase in the thickness of the thermal boundary layer is recorded from X/D=0, the beginning of its appearance. It reaches its maximum value (Y/D=8%) for X/D=6, then it begins to progress parabolically until reaching a value of (Y/D = 20%) for X/D=30. For Tp=35°C, the evolution of the temperature increases until reaching the maximum value of the main flow. While for the other two values T=45°C and Tp=55°C, the evolution of the temperature tends to decrease but with different starting values; the curve of the first temperature starts at T(δT)/Te=1.018 and reaches the value 1, while for the second value of the temperature; it starts at T(δT) /Te=1.05 to reach the same value 1. This difference is due to the difference in the amount of heat flux between the two temperatures.

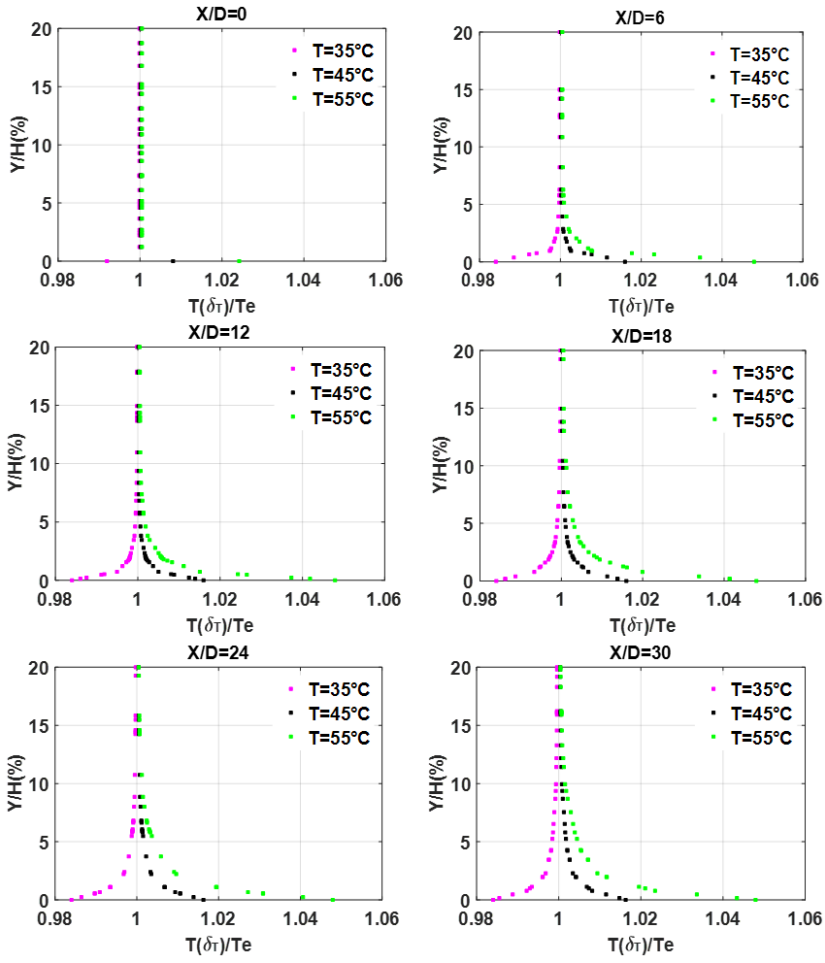

Fig. 13. Temperature profiles for Tp=35°C; Tp=45°C; Tp=55°C.

5.2.3 Static temperature contours for three different flat plate temperatures

In the last step, Fig. 14, the contours of the static temperature are represented. This representation gives us a clear overview of the thickness of the thermal boundary layer. There is a clear difference in the evolution of this boundary layer between the three different temperatures of the wall. For Tp=35°C, the boundary layer starts with a slight variation at the beginning of the plate and then begins to progress slowly to X/D=24 to wait for its maximum value at X/D=30. Concerning the two other values of Tp, one inscribes an almost identical and constant evolution from the beginning of the plate until its end with the clear and very visible remark of the height of this boundary layer which appears bigger in the case of Tp=55°C.

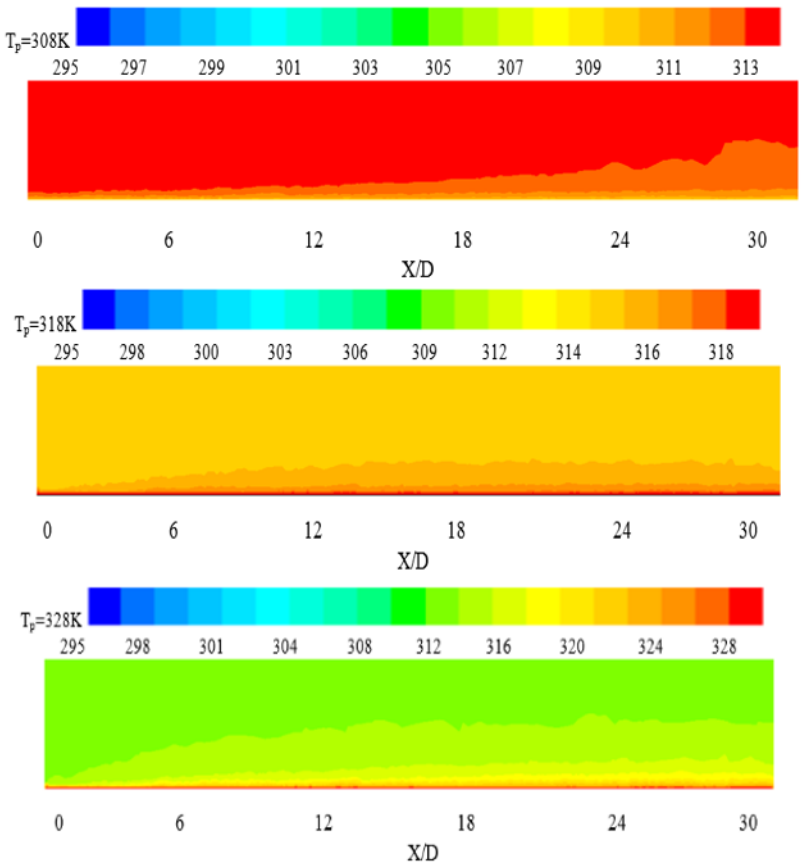

Fig. 14. Temperature contours for Tp=35°C; Tp=45°C; Tp=55°C.

6. Conclusions

The experimental and numerical investigations conducted in this study were performed on a turbulent boundary layer of a flat plate subjected to different heat fluxes. Calculations and tests led to the calculation of some parameters of this boundary layer, such as dynamic and thermal thicknesses.

The inscribed remarks concerning the dynamic thickness δ of the boundary layer indicate that this thickness tends to remain constant at the beginning of the plane plate, and then it begins to

increase in a fast manner with the direction of the flow. From a certain position, the increase of δ is less, but nevertheless reaches a value of 5 mm at the end of the flat plate.

With regard to the thermal thickness θ, a progressive growth of it is registered from the beginning of the plate, the beginning of its appearance, then it begins to progress parabolically until reaching a value of (Y / D = 20%) at the end of the flat plate.

The numerical study tells us about the contours of the static temperature. A clear difference is noticed in the evolution of the thermal boundary layer between the three temperatures of the wall. For Tp = 35 ° C, the boundary layer starts with a slight variation at the beginning of the plate and then begins to progress slowly to reach its maximum value at the end of the plate.

Concerning the two other values Tp=45°C and Tp=55°C, we register a nearly identical and constant evolution from the beginning of the plate until its end with the clear and well-visible note of the height of this boundary layer which appears larger in the case of Tp=55°C.

Acknowledgement The reported work was performed within the ENSMA Schools (P′ institute), the University of Poitiers in France. The welcome received for conducting the experiments is gratefully acknowledged by the author. The author would like to warmly acknowledge Prof. Eva Dorignac and Dr. Gildas Lalizel for their precious and fundamental support in this activity.

References

Mohamad B, Ali M, Neamah H, Zelentsov A, Amroune S (2020). Fluid dynamic and acoustic optimization methodology of a formula-student race car engine exhaust system using multilevel numerical CFD models, Diagnostyka, vol.21, (3), pp. 103-111.

Mohamad B, Károly J, Zelentsov A (2019). Hangtompító akusztikai tervezése hibrid módszerrel, Multidiszciplináris Tudományok vol.9, (4), pp. 548-555.

Kähler CJ, Adrian RJ, Willert CE (1998). Turbulent boundary layer investigations with conventional and stereoscopic Particle Image Velocimetry., Proc. 8th Intl. Symp. Appl. Lazer Tech. Fluid Mech., Lisbon, Portugal, 11.1.1-11.1.8.

White FM (2011). Fluid Mechanics, University of Rhode Island, New York, NY 10020, The McGraw-Hill Companies.

Wallace JM, Eckelmann H, Brodkey RS (1972). The wall region in turbulent shear flow, J. Fluid Mech., vol. 54, pp. 39-48.

Head MR, Bandyopadhyay P (1981). New aspects of turbulent boundary layer structure, J. Fluid Mech., vol. 107, pp. 297-338.

Klebanoff PS (1955). Characteristics of turbulence in a boundary layer with zero pressure gradient, Report 1247, NACA.

Falco RE (1983). New results, a review and synthesis of the mechanism of turbulence production in boundary layers and its modification, AIAA, 83-0377.

Blackwelder RF, Kaplan RE (1976). On the wall structure of turbulent boundary layer, J. Fluid Mech., vol. 76, pp 89-112.

Kline SJ, Reynolds WC, Schraub FA, Runstadler PW (1967). The structure of turbulent boundary layers, J. Fluid Mech., vol. 30, pp. 741-773.

Robinson SK (1991). Coherent motions in the turbulent boundary layer, Annu. Rev. Fluid Mech., vol. 23, pp. 601-639.

Alameri SA, Alkaabi AK (2020). Nuclear Reactor Technology Development and Utilization A volume in Woodhead Publishing Series in Energy Book.

Theodorsen, (1952). Mechanism of turbulence, Proc. Midwest. Conf. Fluid Mech., 2nd, Colombus, Ohio, pp. 1-18.